nature portfolio

https://doi.org/10.1038/s43588-021-00157-1

Supplementary information

How connectivity rules and synaptic properties shape the efficacy of pattern separation in the entorhinal cortex–dentate gyrus–CA3 network

In the format provided by the authors and unedited

Supplementary Information

How connectivity rules and synaptic properties shape the efficacy of pattern separation in the entorhinal cortex–dentate gyrus–CA3 network

S. Jose Guzman[1,2,] Alois Schlögl[1], Claudia Espinoza[1,3], Xiaomin Zhang[1,4], Benjamin A. Suter[1], and Peter Jonas[1,*]

1 IST Austria (Institute of Science and Technology Austria), Am Campus 1, A-3400 Klosterneuburg, Austria

2 Present address: Institute for Molecular Biotechnology (IMBA), Dr. Bohr-Gasse 3, A-1030 Wien, Austria

3 Present address: Medical University of Vienna (MUW) Austria, Division of Cognitive Neurobiology, Spitalgasse 4, A-1090 Wien, Austria

4 Present address: Brain Research Institute, University of Zürich, Winterthurerstrasse 190, CH-8057 Zürich, Switzerland

* Corresponding author. E-mail: peter.jonas@ist.ac.at

Supplementary Figure 1 | Schematic illustration of full-scale network simulations.

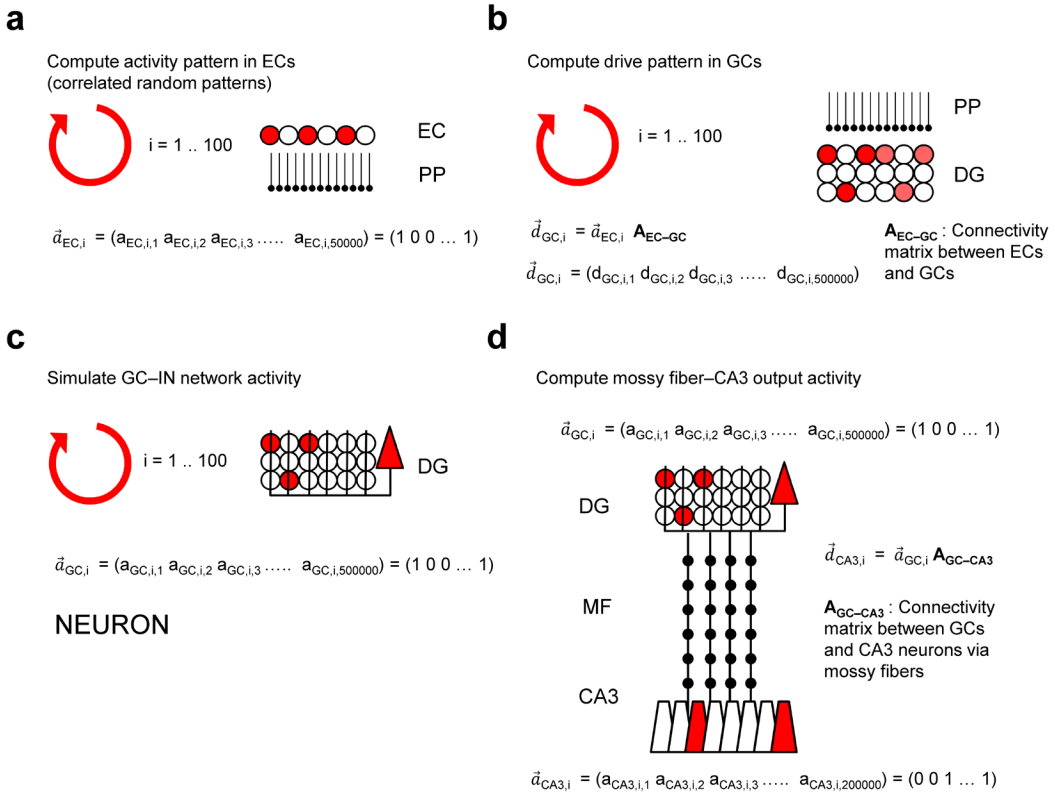

a, Computation of activity in EC cells. $\vec{a}_{EC,i}$ represents the i[th] binary activity vector in the EC population (50,000 neurons).

b, Computation of drive patterns in GCs. $\vec{d}_{GC,i}$ represents the i[th] drive vector in GCs (500,000 neurons). $\vec{d}_{GC,i}$ was computed as the product of activity vector $\vec{a}_{EC,i}$ and connectivity matrix $\mathbf{A}_{EC-GC}$. PP, perforant path.

c, Computation of activity in the DG. Activity in the full-size network was simulated using NEURON version 7.6.2, 7.7.2, or 7.8.2 (Carnevale & Hines, 2006). $\vec{a}_{GC,i}$ represents the i[th] binary activity vector in the GCs, determined by the spiking of GCs.

d, Computation of activity in the CA3 region. $\vec{a}_{CA3,i}$ represents the i[th] binary activity vector in the CA3 pyramidal neurons (200,000 neurons), determined by the spiking of the CA3 cells. MF, mossy fiber.

Correlations R_{in} were computed between pairs of drive vectors, correlations R_{out} were computed between pairs of activity vectors. Finally, R_{out} and R_{in} values were plotted against each other, and a continuous function $f(x)$ was obtained by interpolation.

Supplementary Figure 2 | Pattern separation in a network model with conductance-based single-compartment GCs.

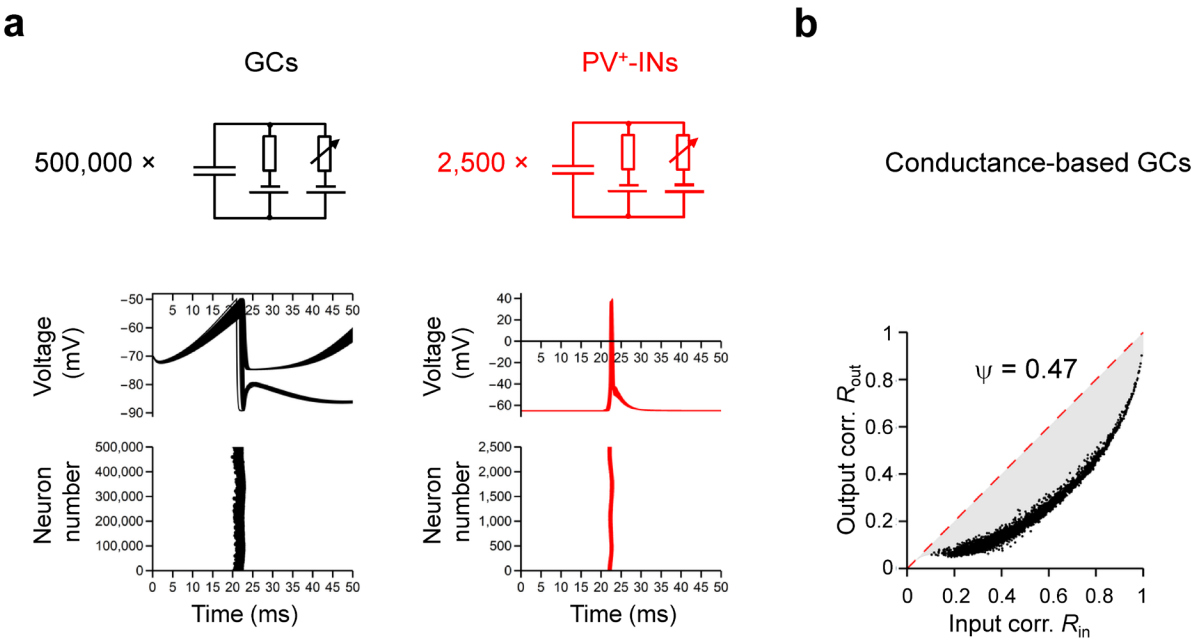

a, Simulated membrane potentials (top) and rasterplots of PN and IN firing (bottom) in a model in which both GCs and PV$^+$-INs were represented by conductance-based single-compartment models (insets). Every point in the rasterplots represents an AP.

b, R_{out}–R_{in} curve in a model with conductance-based synapses. Note that pattern separation efficacy was similar to that of the standard model with current-based synapses. In GCs, g_L was set to 0.05 mS cm^{-2} and C_m was set to 1 µF cm^{-2}, resulting in a membrane time constant of 50 ms. For the inhibitory synaptic conductance, we chose $\tau_{rise,I}$ = 0.1 ms, $\tau_{decay,I}$ = 5 ms, and a peak conductance of 10 nS. The resting potential was set to −70 mV, the synaptic reversal potential was −75 mV, and the AP threshold was set to −50 mV. Once the threshold was exceeded, an afterhyperpolarization conductance was triggered (reversal potential −90 mV; decay time constant 17 ms, peak conductance 500 nS, i.e. 50 times larger than the unitary synaptic conductance). Driving current I_μ was set to 200 pA.

Supplementary Figure 3 | Pattern separation in a network model activated by Poisson train input.

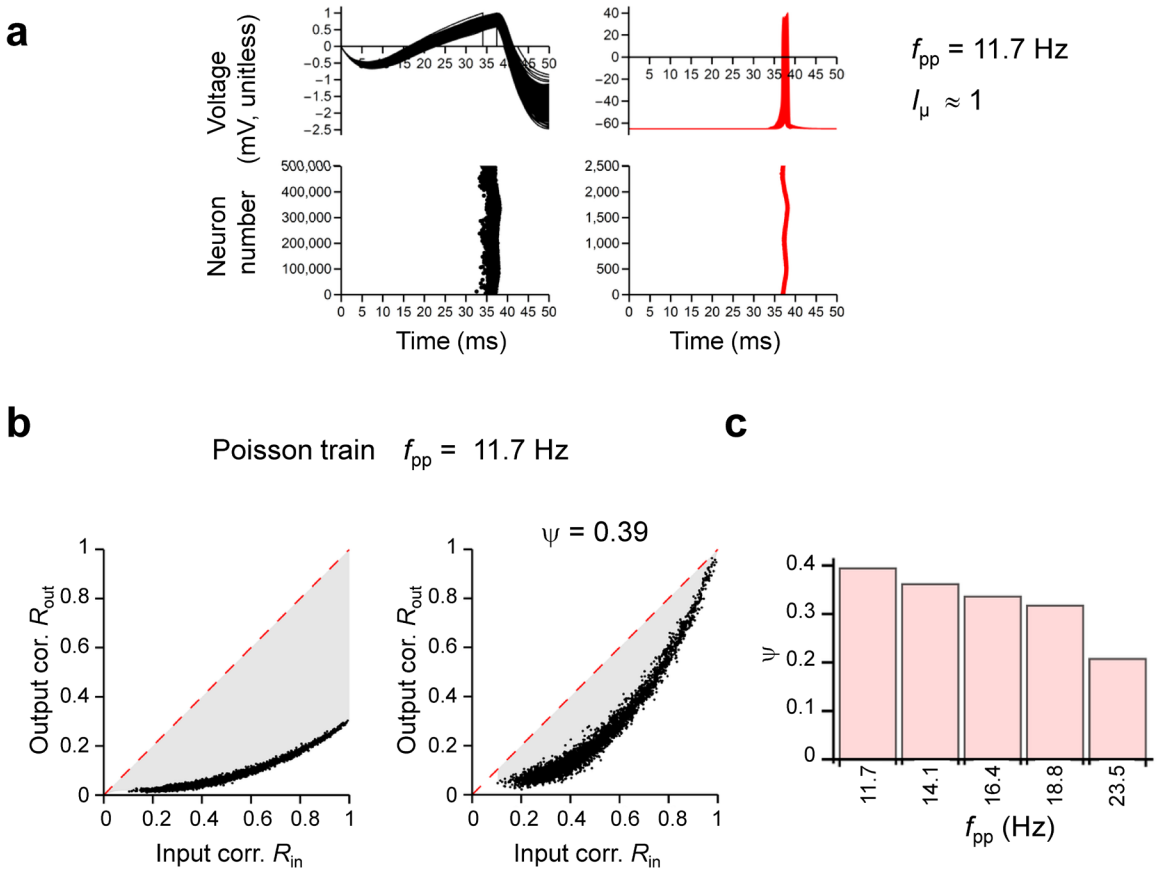

a, Simulated membrane potentials (top) and rasterplot of PN and IN firing (bottom) in a model with EC–GC synaptic input represented by Poisson trains of APs at different frequency. Every point in the rasterplots represents an AP. Average activity frequency of the PP synapses f_{pp} = 11.7 Hz; activation frequency was chosen to give $I_\mu \approx 1$.

b, R_{out}–R_{in} curve for a model in which excitatory drive was generated by Poisson trains of EPSCs in GCs (right; f_{pp} = 11.7 Hz, corresponding to $I_\mu \approx 1$). Left, original R_{out}–R_{in} data; R_{out} becomes reduced because an additional randomization process was added to the system. Right, normalized R_{out}–R_{in} data, in which R_{out} was normalized to the value in which identical input patterns were applied (R_{in} = 1).

c, Dependence of ψ from normalized R_{out}–R_{in} curves on activity frequency of perforant path synapses. Synaptic weight of EC–GC synapses was set to J_{EC-GC} = 0.002 in all simulations. Activation frequency was chosen to approximately match I_{μ} = 1, 1.2, 1.4, 1.6, and 2.0 in the standard model.

Supplementary Figure 4 | Effects of spatial input correlation on pattern separation.

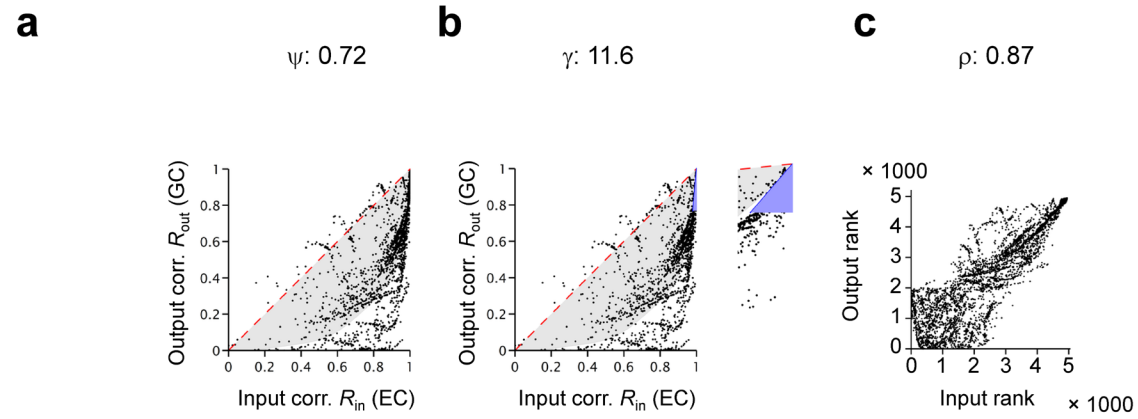

a, b, R_{out}–R_{in} curves and (**c**) rank correlation plot for spatially correlated input patterns. Spatial correlation in EC patterns (50,000 cells) was defined by an exponential function with a length constant of 15,000 cells. Note that both ψ and γ were comparable between simulations with spatially correlated patterns and random patterns (Figure 2c), indicating that the pattern separation mechanism was preserved. In contrast, rank correlation (ρ) was reduced, because of the structure of the correlated patterns. Spatially correlated patterns were generated by random numbers drawn from a multinormal distribution and thresholded to give a binary pattern with appropriate activity level.

Supplementary Figure 5 | Pattern separation in a network model with feedforward inhibition.

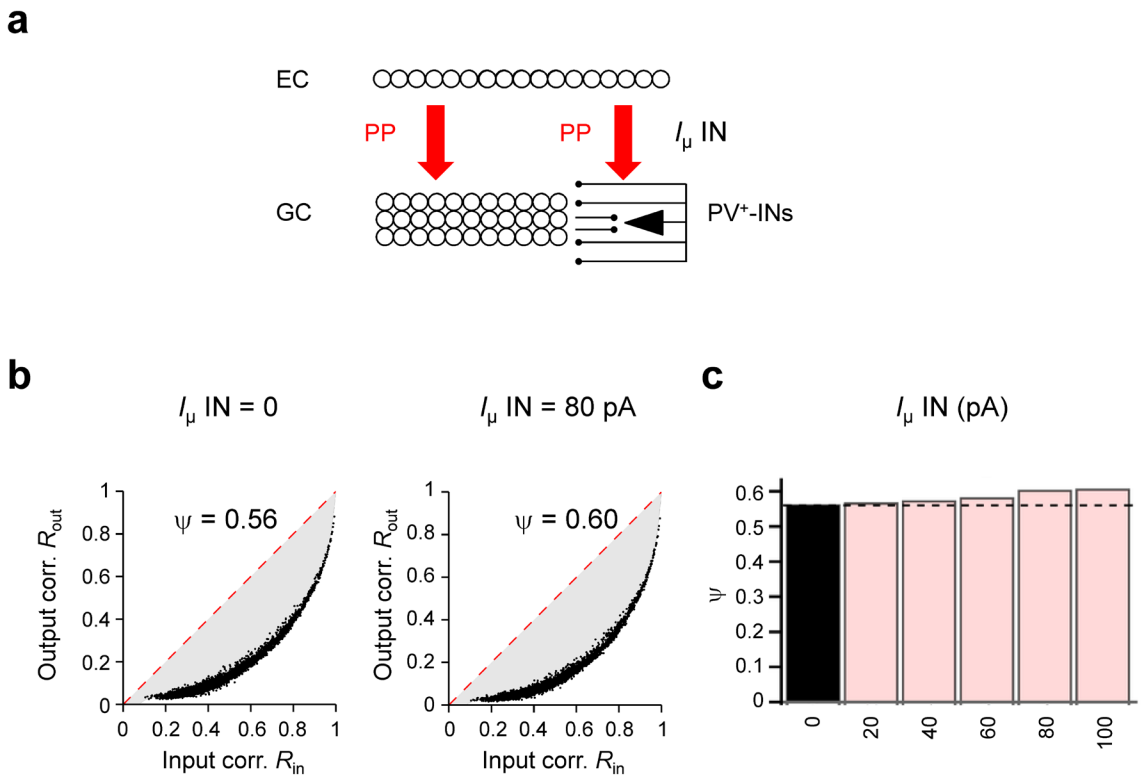

a, Schematic illustration of the network model incorporating feedforward inhibition, in addition to feedback inhibition. ECs innervate GCs and INs with similar connectivity rules. The tonic excitatory drive in an individual IN was computed from the drive from the nearest GC as:

$I_{\mu I}[i] = I_{\mu E}[i/n_I \times n_E] / \langle I_{\mu E} \rangle \times I_{\mu,I}$, $i = 1 \ldots n_I$,

where $I_{\mu I}[i]$ is the excitatory drive in the i^{th} IN (unitless), $I_{\mu E}[i]$ is the excitatory drive in the i^{th} GC, n_I is the number of INs, n_E is the number of GCs, $\langle I_{\mu E} \rangle$ is the average excitatory drive over all GCs, and $I_{\mu,I}$ is the chosen excitatory drive in the INs (in pA).

b, Input-output correlation graphs in a control network (left) and a network incorporating feedforward drive to INs (right).

c, Dependence of ψ on feedforward drive in INs. Black bar, default value (no feedforward excitatory drive on INs); light red bars, larger values (increased feedforward excitatory drive on INs). Note that the pattern separation index ψ is slightly increased by incorporation of feedforward inhibition.

Supplementary Figure 6 | Effects of CCK⁺-like interneurons on pattern separation.

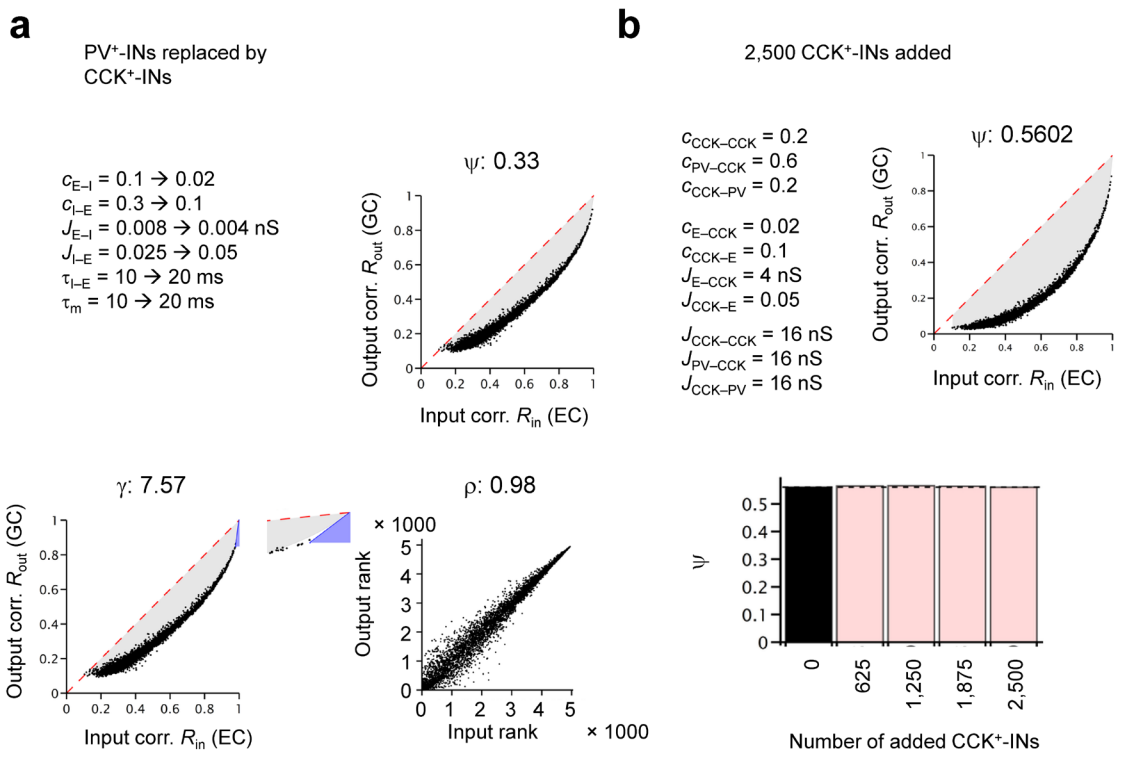

a, Effects of completely replacing PV⁺-like INs by CCK⁺-like INs. Connectivity, synaptic strength, and signaling speed were changed (arrows) according to experimental data (Hefft & Jonas, 2005; Armstrong & Soltesz, 2012; Espinoza et al., 2018). Both ψ and γ decreased in comparison to networks with PV⁺-INs (Figure 2c).

b, Effects of adding CCK⁺-like INs. Top, R_{out}–R_{in} curve after addition of 2,500 CCK⁺-like INs to the network. Bottom, summary bar graph of ψ for R_{out}–R_{in} data for different numbers of CCK⁺-INs added to the network. Note that introducing CCK⁺-INs has only minimal effects on pattern separation performance, although CCK⁺-INs were connected to both GCs and PV⁺-INs (see inset for connectivity and efficacy parameters).

Supplementary Figure 7 | Pattern separation in a network model with type 1 and type 2 synaptic amplitude variability.

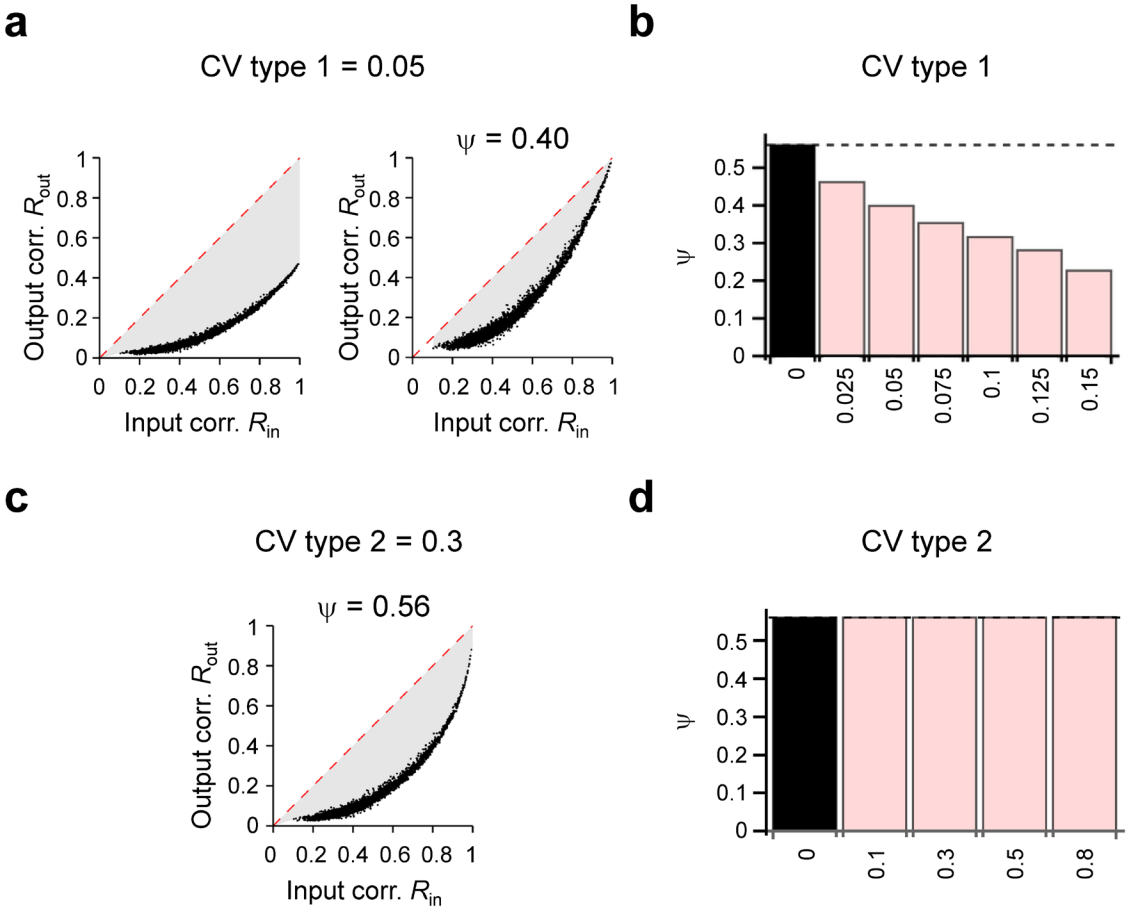

a, b, ψ for different degrees of type 1 (trial-to-trial) variability in the amplitude of all synapses (excitatory E–I, inhibitory I–E, and inhibitory I–I synapses). Coefficient of variation of unitary synaptic strength (CV = standard deviation / mean) was varied between 0.025 and 0.15. The synaptic weights fluctuated randomly from trial to trial. Top, R_{out} – R_{in} curves for CV = 0.05. Left, original R_{out}–R_{in} data; R_{out} becomes reduced because an additional randomization process was added to the system. Right, normalized R_{out}–R_{in} data, in which R_{out} was normalized to the value in which identical input patterns were applied (R_{in} = 1). Bottom, summary bar graph of ψ from normalized R_{out}–R_{in} data.

c, d, Similar analysis as shown in (a), but for type 2 variability. ψ for different degrees of type 2 (synapse-to-synapse) variability in the amplitude of all synapses (excitatory E–I, inhibitory I–E, and inhibitory I–I synapses). Coefficient of variation (CV = standard

deviation / mean) was varied between 0.1 and 0.8. The synaptic weights differed between individual synapses, but were constant from trial to trial. Note that type 2 variability has only minimal effects on pattern separation.

Supplementary Figure 8 | Effects of heterogeneity of intrinsic GC excitability on pattern separation.

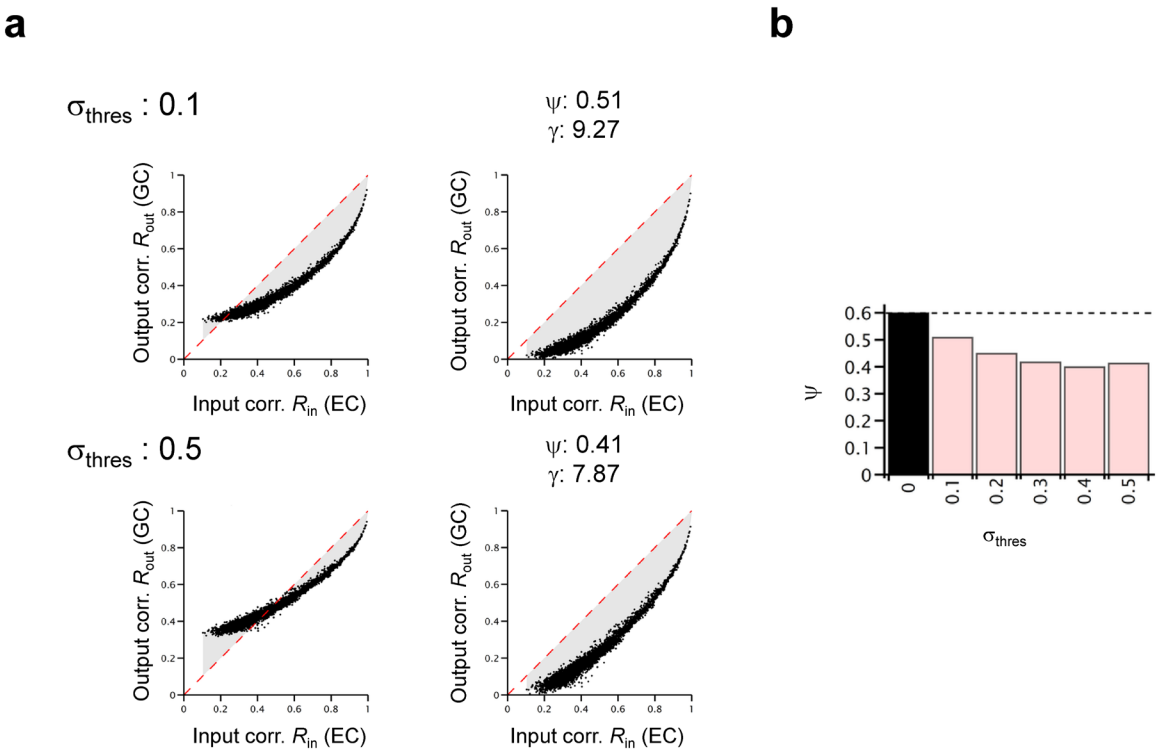

a, R_{out}–R_{in} curves for standard deviation of threshold of GCs σ_{thres} = 0.1 (top) and σ_{thres} = 0.5 (bottom). As GCs are implemented as integrate-and-fire neurons, the default threshold value is one. Left, original R_{out}–R_{in} data; R_{out} approaches values > 0 for R_{in} → 0, because activity was biased towards the cells with low-threshold, independent of pattern variability. Right, normalized R_{out}–R_{in} data, in which R_{out} was scaled so that the minimum value approached 0.

b, Summary bar graph of ψ for normalized R_{out}–R_{in} data for different σ_{thres} values. Note that introducing heterogeneity reduces pattern separation performance.

Supplementary Figure 9 | Effects of fast axonal signaling and delay compensation on pattern separation.

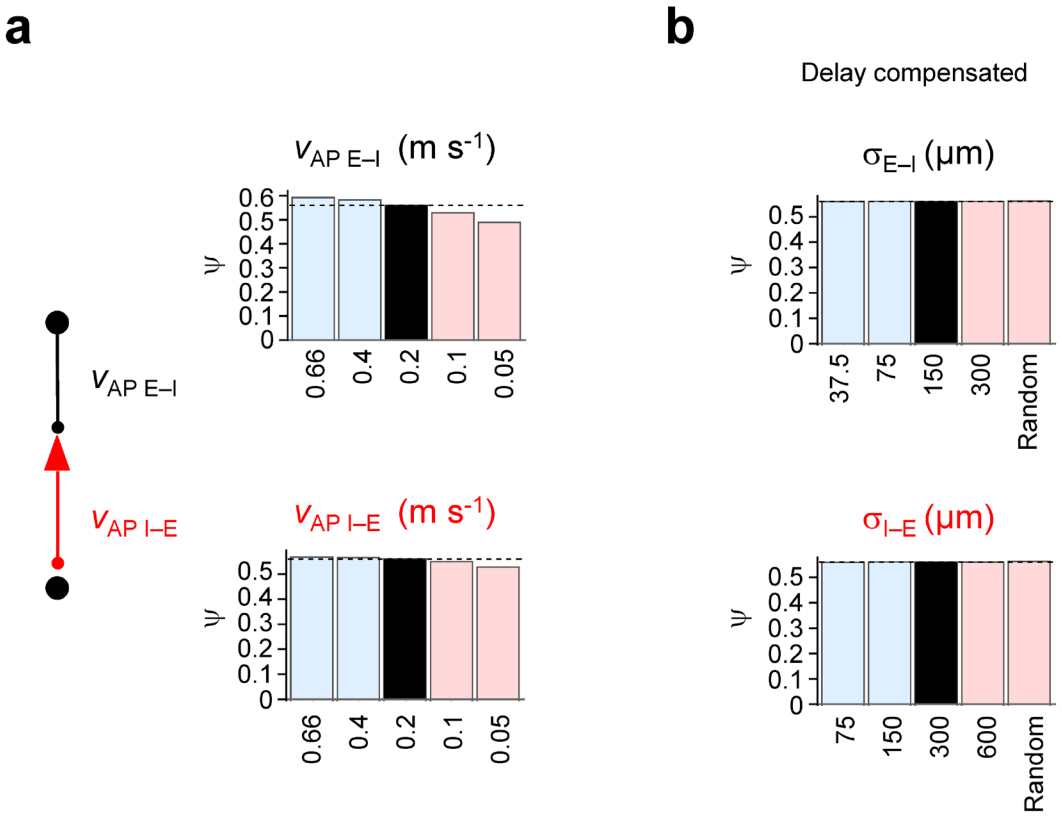

a, Summary bar graph of pattern separation index ψ for different AP propagation velocity values for excitatory GC–PV$^+$-IN synapses ($v_{AP\ E–I}$, top) and inhibitory PV$^+$-IN–GC synapses ($v_{AP\ I–E}$, bottom).

b, Summary bar graph of ψ for different values of excitatory $\sigma_{E–I}$ (top) or inhibitory $\sigma_{I–E}$ (bottom) connectivity after compensatory adjustment of both connectivity and delay to maintain both total connectivity and average delay at their default values. Note that broadening of connectivity fails to reduce pattern separation performance in the presence of delay adjustment (unlike in Figure 5b). Thus, the beneficial effects of local connectivity are largely generated via faster signaling.

Supplementary Table 1 | Standard parameters for the full-scale EC–DG–CA3 network model of pattern separation.

Parameter	Meaning	Standard value (range)	References
n_{EC}	number of entorhinal cortex (EC) cells	50,000 (12,500–200,000)	
n_{E}	number of granule cells (GCs)	500,000	Amrein et al., 2004
n_{I}	number of PV^+ interneurons (PV^+-INs)	2,500	Marr & Jonas, unpublished
n_{CA3}	number of CA3 pyramidal neurons	200,000	Boss et al., 1987
$c_{E–I}$	maximal connection probability E–I synapses	0.1 (a)	Espinoza et al., 2018
$\sigma_{E–I}$	connection width E–I synapses	150 µm (37.5–300 µm) (b)	Espinoza et al., 2018
$J_{E–I}$	synaptic strength E–I synapses	8 nS (2–32 nS) (c)	Geiger et al., 1997
$\tau_{rise,E}$	EPSC rise time constant	0.1 ms	Geiger et al., 1997
$\tau_{decay,E}$	EPSC decay time constant	1 ms	Geiger et al., 1997
$c_{I–E}$	maximal connection probability I–E synapses	0.3 (a)	Espinoza et al., 2018
$\sigma_{I–E}$	connection width I–E synapses	300 µm (75–600 µm) (b)	Espinoza et al., 2018

J_{I-E}	synaptic strength I–E synapses	0.025 (0.005–0.1) (d)	Kraushaar & Jonas, 2000
τ_{I-E}	IPSC decay time constant	10 ms	Kraushaar & Jonas, 2000
c_{I-I}	maximal connection probability I–I synapses	0.6	Espinoza et al., 2018
σ_{I-I}	connection width I–I synapses	300 µm (b)	Espinoza et al., 2018
J_{I-I}	synaptic strength I–I synapses	16 nS	Bartos et al., 2001; 2002
τ_{I-I}	IPSC decay time constant	2.5 ms	Bartos et al., 2001; 2002
$v_{AP,E-I}$, $v_{AP,I-E}$	axonal AP propagation velocity	0.2 m s^{-1} (0.05–0.66 m s^{-1}) (e)	Hu & Jonas, 2014; Doischer et al., 2008; Schmidt-Hieber et al., 2008
$\delta_{syn,E}$, $\delta_{syn,I}$	extra synaptic delay	0 ms (0–2 ms)	Geiger et al., 1997; Kraushaar & Jonas, 2000
J_{gamma}	external inhibitory gamma-frequency drive to GCs	1.0 (0.5–3.5) (d)	de Almeida et al., 2009
c_{gap}	maximal connection probability gap junctions	0.8	Espinoza et al., 2018
σ_{gap}	connection width gap junctions	150 µm (b)	Espinoza et al., 2018

R_{gap}	gap junction resistance	300 MΩ	Bartos et al., 2001
$c_{EC\text{-}GC}$	maximal connection probability EC–GC synapses	0.2 (0.05–1)	Tamamaki & Nojyo, 1993; Steward, 1976; Witter, 2007; Desmond & Lavy, 1985
$\sigma_{EC\text{-}GC}$	connection width EC–GC synapses	500 µm (50 µm–infinity)	Tamamaki & Nojyo, 1993; Steward, 1976; Witter, 2007; Desmond & Lavy, 1985
α_{EC}	average activity in EC neurons	0.1 (0.02–0.5) (d)	Schmidt-Hieber & Häusser, 2013
I_{μ}	amplitude of excitatory drive in GCs	1.8 (1.0–2.0) (e)	
$J_{GC–CA3}$	synaptic strength GC–CA3 mossy fiber synapses	0.34 (0.15–1.01) (e)	Vyleta et al., 2016
n_{MFBs}	number of mossy fiber boutons per GC axon	15	Amaral et al., 1990; Acsády et al., 1998
σ_{nMFBs}	standard deviation of number of mossy fiber boutons per GC axon	5 (0–15)	

$\sigma_{GC–CA3}$	connection width GC–CA3 synapses	500 µm (0–5 mm)	
$v_{AP,GC–CA3}$	axonal AP propagation velocity mossy fiber axons	0.2 m s^{-1} (g)	Jonas et al., 1993; Vandael et al., 2020
δ_{GC-CA3}	extra delay GC–CA3 mossy fiber synapses (f)	4 ms	Jonas et al., 1993; Vandael et al., 2020

(a) For the standard parameter set, the ratio of inhibitory to excitatory synapses was 6, consistent with the experimental data (Espinoza et al., 2018).
(b) Space constants refer to a total length of the hippocampal formation of 5 mm.
(c) Firing threshold of PV^+-INs was ~18 nS.
(d) Activity of EC neurons can be roughly estimated as the ratio of AP frequency to gamma oscillation frequency.
(e) Unitless, because GCs and CA3 pyramidal neurons were modeled as LIF neurons.
(f) For the standard values of $v_{AP,E–I}$, $v_{AP,I–E}$, $\sigma_{E–I}$, and $\sigma_{I–E}$, the weighted mean latency is 0.60 ms for E–I synapses and 1.20 ms for I–E synapses, consistent with experimental observations (Espinoza et al., 2018).
(g) Set larger than synaptic delay to account for additional conduction time, corresponding to distance between DG and proximal CA3 region.

Values in parentheses indicate explored parameter range. EPSC, excitatory postsynaptic current; IPSC, inhibitory postsynaptic current; AP, action potential.

Supplementary References

78. Doischer, D., Hosp, J.A., Yanagawa, Y., Obata, K., Jonas, P., Vida, I., & Bartos, M. Postnatal differentiation of basket cells from slow to fast signaling devices. *Journal of Neuroscience* **28**, 12956–12968 (2008).

79. Schmidt-Hieber, C., Jonas, P., & Bischofberger, J. Action potential initiation and propagation in hippocampal mossy fibre axons. *Journal of Physiology* **586**, 1849–1857 (2008).

80. Desmond, N.L., & Levy, W.B. Granule cell dendritic spine density in the rat hippocampus varies with spine shape and location. *Neuroscience Letters* **54**, 219–224 (1985).

81. Schmidt-Hieber, C., & Häusser, M. Cellular mechanisms of spatial navigation in the medial entorhinal cortex. *Nature Neuroscience* **16**, 325–331 (2013).

82. Acsády, L., Kamondi, A., Sík, A., Freund, T., & Buzsáki, G. GABAergic cells are the major postsynaptic targets of mossy fibers in the rat hippocampus. *Journal of Neuroscience* **18**, 3386–3403 (1998).

83. Jonas, P., Major, G., & Sakmann, B. Quantal components of unitary EPSCs at the mossy fibre synapse on CA3 pyramidal cells of rat hippocampus. *Journal of Physiology* **472**, 615–663 (1993).